Spatial correlation in matter-wave interference as a measure of decoherence, dephasing, and entropy

Zilin Chen, Peter Beierle, and Herman Batelaan
Department of Physics and Astronomy, University of Nebraska-Lincoln, 208 Jorgensen Hall, Lincoln, Nebraska 68588-0299, USA

(Received 20 October 2017; published 9 April 2018)

The loss of contrast in double-slit electron diffraction due to dephasing and decoherence processes is studied. It is shown that the spatial intensity correlation function of diffraction patterns can be used to distinguish between dephasing and decoherence. This establishes a measure of time reversibility that does not require the determination of coherence terms of the density matrix, while von Neumann entropy, another measure of time reversibility, does require coherence terms. This technique is exciting in view of the need to understand and control the detrimental experimental effect of contrast loss and for fundamental studies on the transition from the classical to the quantum regime.

DOI: 10.1103/PhysRevA.97.043608

In optical and matter-wave interferometry a loss of contrast is a limit on the detection capability of such devices. Loss of contrast can be attributed to physical processes divided into two broad classes. Dephasing processes are time reversible, whereas decoherence processes are time irreversible. Time reversibility can be established by evaluating the change in entropy, $S = -\mathrm{Tr}\rho \ln \rho$, where ρ is the density matrix describing the physical system. When S remains constant in time, the process is time reversible; when it increases in time, the process is time irreversible [1]. The value of the entropy depends on the off-diagonal or coherence terms of the density matrix, which is apparent from the calculation of the entropy using the spectral decomposition $S = -\sum \lambda_i \ln \lambda_i$, where λ_i are the eigenvalues of the density matrix. In diffraction experiments, determination of the coherence terms would require special techniques, such as quantum-state tomography [2]. Thus, the on-diagonal terms of the density matrix, which describes the spatial probability distribution of the physical system, do not appear to provide direct access to the very nature of the process that is limiting the contrast observed in that probability distribution. This makes it hard to identify sources of contrast loss and thus to take appropriate measures to reduce such a loss. Additionally, when studying the transition from the quantum to the classical domain, by introducing controlled decoherence processes, it is hard to establish that it is indeed decoherence and not dephasing that causes a loss of contrast.

In this paper, we propose and analyze a method based on repetitive measurements of the spatial probability distributions, which can be used to distinguish dephasing from decoherence processes. The spatial second-order (also called intensity) correlation function of the measurements provides this information. For dephasing processes that upon visual inspection appear to completely destroy the diffraction pattern, the intensity correlation function restores the far-field diffraction pattern. For decoherence processes no such restoration works.

To support our claims, we consider an electron double-slit experiment [3,4] as an archetypical example of an interference experiment, and add a process by which contrast is lost. This situation described is not just a thought experiment, but is typical for physical experiments. For example, we reported an electron-diffraction experiment with nanofabricated gratings, where some loss of contrast was observed and modeled [4].

An optical experiment that exhibited loss of contrast was performed by Rui-Feng *et al.* [5]. In their setup, a laser beam with a 632.8-nm wavelength passed through a ground glass disk and double slits. The detection screen was placed in the Fresnel diffraction region with respect to the double slits. The ground glass disk appeared to completely destroy the contrast of the diffraction pattern. The normalized intensity correlation function was used to regain the double-slit diffraction pattern. This is a striking result in its own right. The central question which was not addressed is, How can we detect if an object dephases or decoheres the laser light? Of course, a ground glass disk dephases, but if we had an unknown interaction, could we tell from diffractive noisy images the difference? Or in general, Can spatial correlation be used to identify dephasing and decoherence processes?

In our simulation, we studied the analogous double-slit physical system but changed the diffracting particle from photons to electrons as decoherence theory is often studied in the context of matter optics [6–11]. Based on the matter-wave analogy [12] the method is expected to work for both matter waves and optics. Our approach is to simulate electron diffraction in three different situations as shown in Fig. 1. In the first situation, a two-path interferometer, i.e., a double-slit experiment, exhibits excellent contrast. In the second and third situations, an object is introduced after the double slit that interacts with the electron wave so as to cause dephasing or decoherence. We refer to this as a "dephaser" and "decoherer." These latter two patterns share a reduced contrast but are found to have qualitatively different intensity correlation functions.

The example physical system we study (Fig. 2) is motivated by previously used experimental parameters for electron double-slit and decoherence experiments [10,18]. A coherent electron wave with an energy of $E = 1670$ eV and a transverse width of $w_0 = 15\ \mu$m at the source propagates $L_1 = 24$ cm and encounters a double slit. A dephaser or decoherer is located immediately after the double slit, represented by a horizontal surface. The size of the surface and the double slit are both

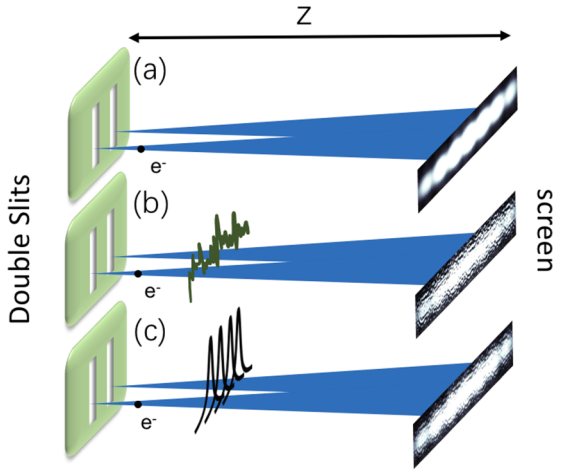

FIG. 1. Dephasing versus decoherence. A sketch of three situations where electron waves interfere. (a) Electron waves are unaffected. An interference pattern will be observed in the probability distribution with excellent contrast. The observed pattern is taken from Bach *et al.* [4]. (b) A "dephaser," represented by a random potential distribution (green wiggly line), adds a position-dependent phase to the electron wave. As a result, the diffraction pattern appears to be washed out, but information about the diffraction pattern can be recovered. (c) A "decoherer" separates the electron wave into a probabilistic sum of several Gaussian waves in addition to a random potential distribution. A low-contrast diffraction pattern similar to (b) is obtained, but now the pattern cannot be recovered.

chosen to be 500 nm wide, larger than the distance between the center of the two slits (150 nm). The width of the slits is $d = 50$ nm. Electrons are diffracted and dephased or decohered and continue to propagate to the detection screen at a distance $L_2 = 25$ cm. An interference pattern can be found on the detection screen which is placed in the far-field region (or in the Fresnel diffraction region with respect to the double slits but far-field region with respect the single slit, as in [5]).

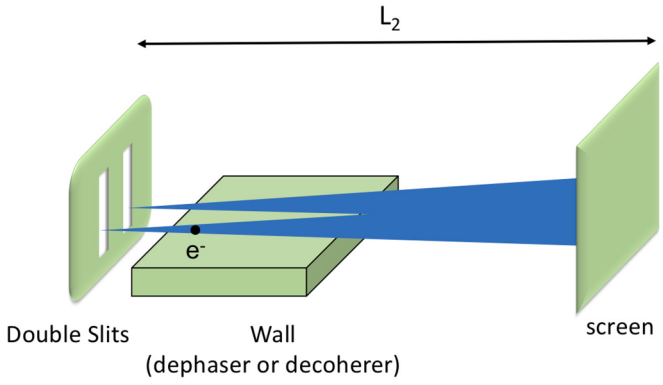

FIG. 2. Schematic of the physical system. An electron wave impinges on a double slit. Subsequently, a dephaser or decoherer disturbs the electron wave. The corresponding real phenomenon is plausibly caused by the back-action of the image charge on the electron [10,13–17].

Propagation of the electron wave is simulated using the path-integral method [12,19],

$$\psi_b(x_b) = \int_{-w/2}^{w/2} dx_a \psi_a(x_a) h(x_b,x_a). \tag{1}$$

The state of the wave function $\psi_b(x_b)$ at each location x_b at the double-slit plane has accumulated a phase attribution from the state of the wave function $\psi_a(x_a) = 1$ at each location x_a on the source according to $h(x_b,x_a)$. Subsequently, the wave function $\psi_b(x_b)$ is modified by the dephaser or decoherer to be $\psi_c(x_b)$ and finally propagated in the same process described in Eq. (1) from the double slit to the detection screen and noted as $\psi_s(x_s)$. For the impulse response function [20]

$$h(x,x') = e^{i2\pi l/\lambda} T(x') \tag{2}$$

in Eq. (1), $l = \sqrt{(x-x')^2 + z^2}$ is the propagation length, z is either L_1 or L_2, and $\lambda = h/\sqrt{2mE}$ is the de Broglie electron wavelength. This function is given in terms of the transmission function $T(x')$. The transmission function equals 1 for the case that the electron propagates from the source to the double slit, $T(x') = T(x_a) = 1$. After passing through the double slit, the transmission function will become the double-slit transmission function

$$T(x') = T(x_b) = D(x_b), \tag{3}$$

which equals 1 at the slits, and zero elsewhere.

The dephaser is simulated by applying a smooth random potential phase $\theta(x_b)$ onto the wave function in the form of $\psi_c(x_b) = \psi_b(x_b) e^{i\theta(x_b)}$ at the double slit. The random phase is given by a sum of Gaussians,

$$\theta(x_b) = \sum_i A_i e^{-\left(\frac{x_b - x_i}{\sqrt{2}\sigma_i}\right)^2}, \tag{4}$$

where A_i are uniformly distributed random numbers ranging from zero to 2π. The Gaussian widths σ_i are random numbers with a normal distribution. The mean value of σ_i is chosen at 4 nm, and its standard deviation is 1 nm for our numerical example. The set of coordinates of centers $\{x_i\}$ are uniformly distributed random positions covering the double slit. Thus, to realize this dephaser, 500 different Gaussian distributions of ~4 nm width are combined [18]. The spacing of the random Gaussians is much smaller than slit width (50 nm) and results in a probability distribution that is spread all over the detection screen.

To describe the decoherer, the wave front is cut into n independent overlapping Gaussians, $\varphi_n(x_b)$, effectively reducing the tranverse coherence length, w, to the width of the Gaussian, σ_i. The Gaussians are propagated separately to find the wave functions $f_n(x_s)$ at the detection screen location. The density matrix before the decoherer is given by

$$\rho_i(x_b,x_b') = \sum_{n=1,N} \frac{1}{N} \varphi_n(x_b) \varphi_n^*(x_b'), \tag{5}$$

with

$$\varphi_n(x_b) = \sqrt{N} \psi_b(x_b) e^{i\theta(x_b)} e^{-\left(\frac{x_b - x_n}{\sqrt{2}\delta_0}\right)^2}. \tag{6}$$

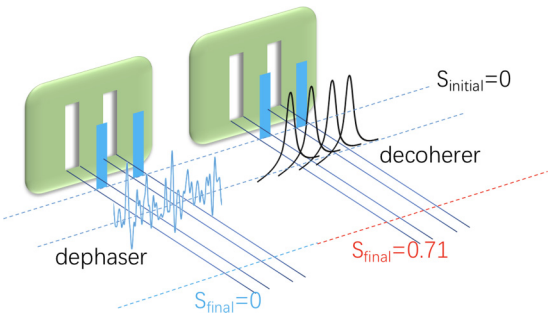

FIG. 3. Entropy. Schematic representation of the decoherer and dephaser in the simulation. The blue vertical lines show the electron wave front after passage through the double slit. The Gaussians represent a sample of four incoherent waves emerging from the decoherer. The blue curve is a sample of the smooth random potential added to the electron wave for both the dephaser and the decoherer. The entropy before and after the dephaser and decoherer is indicated.

The normalization constant N is the same for each Gaussian, $\psi_b(x_b)$ is the wave front on the double slit before the decoherer, and δ_0 is a constant width of 100 nm. Each Gaussian is shifted by $x_n = nx_0$, with $x_0 = 12.5$ nm. Additionally, the same smooth potential phase shift $e^{i\theta(x_b)}$ described in Eq. (4) is applied. The final density matrix is given by

$$\rho_f(x_s,x_s') = \sum_{n=1,N} \frac{1}{N} f_n(x_s) f_n^*(x_s'). \tag{7}$$

The von Neumann entropy is calculated from $S = -\sum \lambda_i \ln \lambda_i$, where λ_i are the eigenvalues of the density matrix. The initial entropy for the pure state is $S = 0$. The effect of the decoherer is to reduce the absolute value of the off-diagonal matrix elements in the density matrix. Consequently, for the dephaser the entropy remains the same, whereas for the decoherer the entropy increases (Fig. 3).

The dependence of the von Neumann entropy on the transverse coherence length, w, after the decoherer is determined and compared to the Shannon entropy. To do this, the Gaussians' widths and centers were varied, keeping their ratio fixed. A narrower width describes more decoherence and yields larger entropy and vice versa. A simpler decoherer model is added for comparison. In this model, the overlapping Gaussian functions are replaced with adjacent nonoverlapping top-hat functions. The Shannon entropy, $S = -\sum p_i \ln p_i$, for this simpler decoherer can be calculated analytically and compared to the computer-simulated von Neumann entropy. Here, p_i, is the probability to land within one top-hat function. When the two slits are covered with N top-hat functions, the probability for an electron to be found within one of the top hats is $p_i = w/2d$. The corresponding Shannon entropy is $S = -\sum p_i \ln p_i = \ln(w/2d)$. The analytic Shannon entropy matches the simulated von Neumann entropy very well (Fig. 4). For the case of Gaussian distributions, the entropy matches that for the top-hat case very well when the widths, w, are smaller than a single slit. As the value of w is increased above the single slit width but remains below the slit separation, the entropy remains relatively constant. When w starts to exceed the separation, the entropy reduces to zero, as expected for a fully coherent state.

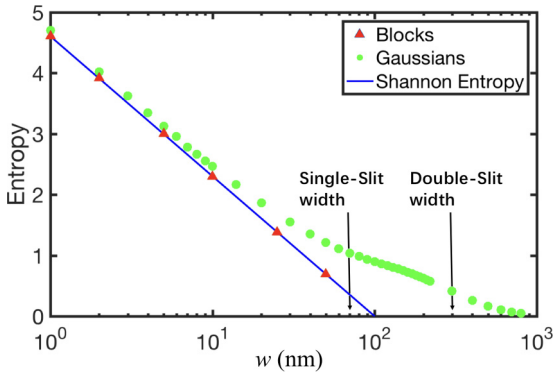

FIG. 4. Transition of entropy. The entropy change is indicated as a function of the transverse coherence length. The von Neumann entropies for the Gaussian model (green circles) and the top-hat model (red triangles) are compared to the Shannon entropy (blue line). The von Neumann entropy and Shannon entropy (blue line) match well for the top-hat model. The Gaussian model matches well for transverse coherence lengths smaller than a single slit. When the transverse coherence length exceeds the slit separation, the entropy approaches zero as expected for a pure state.

Now that we have introduced a dephaser and decoherer, we can proceed to test if a repetitive measurement of the probability distribution can be used to independently determine if a process is due to dephasing or decoherence. To do so, the diffraction pattern was calculated 500 times for both the dephaser and the decoherer. Each realization used a different set of random numbers [in Eq. (4)] to generate a dephaser and decoherer. In Fig. 5, two realizations are shown. In the dephasing realization [Figs. 5(a) and 5(c)], the peaks and valleys are more pronounced than in the decoherer realization [Figs. 5(b) and 5(d)]. This is consistent with earlier work using

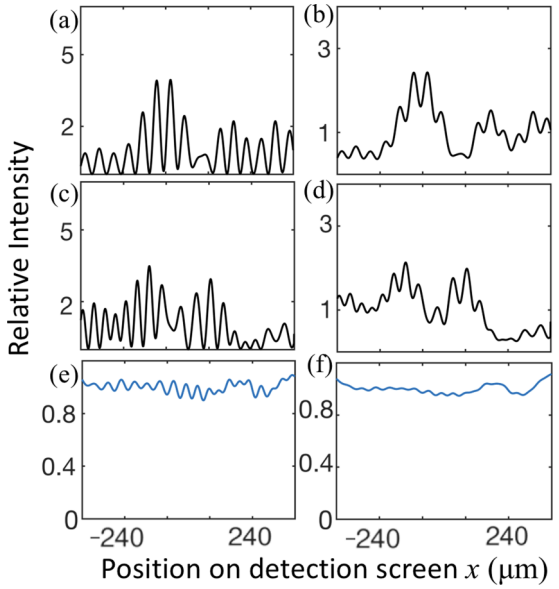

FIG. 5. Simulation realizations: (a, c) two realizations with a dephaser and (b, d) two realizations with a decoherer. In (a, b) and (c, d), the same random numbers are used; thus, the influence of dephaser and decoherer will be more comparable. (e, f) Dephase and decoherer averaged pattern over 500 realizations. The decoherer gives a similar probability distribution to the dephaser but with blurred peaks.

a Wigner function approach [21]. Figures 5(e) and 5(f) are averaged patterns over 500 realizations.

For each probability distribution, the intensity correlation function is calculated. In general, the second-order correlation function is defined as

$$G^{(2)}(x_1,x_2,x_1',x_2') \equiv \langle \psi_1^*(x_1)\psi_2^*(x_2)\psi_1(x_1')\psi_2(x_2')\rangle, \quad (8)$$

from which the intensity correlation function $G^{(2)}(x_{1s},x_{2s}) = \langle I_{1s}(x_{1s})I_{2s}(x_{2s})\rangle$ at the detection screen is obtained. In Eq. (8), $\langle\cdots\rangle$ indicates averaging over time, while in our simulation the averaging is performed over multiple realizations. Following Cheng's derivation [20],

$$\begin{aligned} &G^{(2)}(x_{1s},x_{2s}) \\ &= \int dx_{1b}dx_{2b}dx_{1b}'dx_{2b}' G^{(2)}(x_{1b},x_{2b},x_{1b}',x_{2b}') \\ &\quad \times h_1^*(x_{1s},x_{1b})h_2^*(x_{2s},x_{2b})h_1(x_{1s},x_{1b}')h_2(x_{2s},x_{2b}'). \end{aligned} \quad (9)$$

In Eq. (9), the subscript b represents coordinates at the double slit and s coordinates at the screen. $G^{(2)}(x_{1b},x_{2b},x_{1b}',x_{2b}')$ is the second-order correlation function and contains wave functions at the double slit after the dephasing or decoherence process. This equation describes the propagation of the second-order correlation function from the double slit to the screen.

Applying the result from Goodman [22], $\langle u_1^*u_2^*u_3u_4\rangle \equiv \langle u_1^*u_3\rangle\langle u_2^*u_4\rangle + \langle u_1^*u_4\rangle\langle u_2^*u_3\rangle$, to Eq. (8), a relation between the second-order and first-order correlation functions is obtained,

$$\begin{aligned} G^{(2)}(x_{1b},x_{2b},x_{1b}',x_{2b}') &= G^{(1)}(x_{1b},x_{1b}')G^{(1)}(x_{2b},x_{2b}') \\ &\quad + G^{(1)}(x_{1b},x_{2b}')G^{(1)}(x_{2b},x_{1b}'), \end{aligned} \quad (10)$$

where $G^{(1)}(x_{ib},x_{jb}) \equiv \langle \psi_{ic}{}^*(x_{ib})\psi_{jc}(x_{jb})\rangle$. Substitution of Eq. (10) into Eq. (9) yields

$$\begin{aligned} &G^{(2)}(x_{1s},x_{2s}) \\ &= \left(\int dx_{1b}dx_{1b}' G^{(1)}(x_{1b},x_{1b}')h_1^*(x_{1s},x_{1b})h_1(x_{1s},x_{1b}')\right) \\ &\quad \times \left(\int dx_{2b}dx_{2b}' G^{(1)}(x_{2b},x_{2b}')h_2^*(x_{2s},x_{2b})h_2(x_{2s},x_{2b}')\right) \\ &\quad + \left(\int dx_{1b}dx_{2b}' G^{(1)}(x_{1b},x_{2b}')h_1^*(x_{1s},x_{1b})h_2(x_{2s},x_{2b}')\right) \\ &\quad \times \left(\int dx_{2b}dx_{1b}' G^{(1)}(x_{2b},x_{1b}')h_2^*(x_{2s},x_{2b})h_1(x_{1s},x_{1b}')\right) \\ &= \langle I_{1s}(x_{1s})\rangle\langle I_{2s}(x_{2s})\rangle \\ &\quad + \left|\int dx_{1b}dx_{2b} h_1(x_{1s,}x_{1b})h_2^*(x_{2s,}x_{2b})G^{(1)}(x_{1b},x_{2b})\right|^2. \end{aligned} \quad (11)$$

Therefore, the deviation of the second-order correlation function is

$$\begin{aligned} &\Delta G^{(2)}(x_{1s},x_{2s}) \\ &\equiv G^{(2)}(x_{1s},x_{2s}) - \langle I_{1s}(x_{1s})\rangle\langle I_{2s}(x_{2s})\rangle \\ &\equiv \left|\int dx_{1b}dx_{2b}h_1^*(x_{1s,}x_{1b})h_2(x_{2s,}x_{2b})G^{(1)}(x_{1b},x_{2b})\right|^2. \end{aligned} \quad (12)$$

To evaluate Eq. (12), the impulse response function h can be approximated for $z \gg x - x'$. In this case $l \approx z + \frac{(x-x')}{2z}$, which, applied to Eq. (2), gives

$$h(x,x') = e^{ikz}e^{i\frac{k(x-x')^2}{2z}}T(x'). \quad (13)$$

The random potential phase affects the wave function in such a way that when the integration time is long enough (or the number of realizations is large enough in the simulation), the first-order correlation function $G^{(1)}(x_{1b},x_{2b}) \propto \langle e^{i[\theta(x_{2b})-\theta(x_{1b})]}\rangle$ can be evaluated to give

$$G^{(1)}(x_{1b},x_{2b}) \approx I_0\delta(x_{1b} - x_{2b}). \quad (14)$$

In this evaluation, the random phase we consider in the simulation consists of narrow Gaussians, analogous to the expected effect that a real physical system would have on an electron wave. The δ-function description in Eq. (14) is thus an approximation for the case of narrow Gaussians and is obtained for a pointwise random phase.

Up to this point, no distinction was made between the dephaser and the decoherer. For the dephaser, substitution of Eqs. (13) and (14) into Eq. (12) leads to the deviation

$$\begin{aligned} &\Delta G^{(2)}(x_{1s},x_{2s}) \\ &\equiv \left|\int dx_{1b}dx_{2b}h^*(x_{1s,}x_{1b})h(x_{2s,}x_{2b})G^{(1)}(x_{1b},x_{2b})\right|^2 \\ &= \left|2\pi I_0 e^{ik\frac{(x_{2s}^2-x_{1s}^2)}{2z}}\widetilde{|T|^2}\left(\frac{k}{z}(x_{1s}-x_{2s})\right)\right|^2. \end{aligned} \quad (15)$$

The $\widetilde{|T|^2}$ is the Fourier transformation of $|T|^2$. In the following we drop the subscript "s"; $x_i = x_{is}$ to represent coordinates on the screen. We recall the expression of the transmission function [Eq. (3)] and substitute in Eq. (15) to get

$$\widetilde{T^2}\left(\frac{k}{z}(x_1-x_2)\right) = \widetilde{D^2}\left(\frac{k}{z}(x_1-x_2)\right). \quad (16)$$

Thus, Eq. (15) can be rewritten as

$$\Delta G^{(2)}(x_1,x_2) = \left|2\pi I_0 e^{ik\frac{(x_2^2-x_1^2)}{2z}}\widetilde{D^2}\left(\frac{k}{z}(x_1-x_2)\right)\right|^2. \quad (17)$$

Using the normalized intensity correlation function,

$$\begin{aligned} \Delta g^{(2)}(x_1,x_2) &= \Delta G^{(2)}(x_1,x_2)/(\langle I(x_1)\rangle\langle I(x_2)\rangle) \\ &= \langle I(x_1)I(x_2)\rangle/(\langle I(x_1)\rangle\langle I(x_2)\rangle) - 1, \end{aligned} \quad (18)$$

where $I(x_1)$ represents the intensity at position x_1 on the screen.

We come to a result that

$$\Delta g^{(2)}(x_1,x_2) \propto \left|e^{ik\frac{(x_2^2-x_1^2)}{2z}}\widetilde{D^2}(k_{x_1,x_2})\right|^2, \quad (19)$$

where $k_{x_1,x_2} = k(x_1 - x_2)/z$. In the simulation, symmetric coordinates are chosen in the x axis, $x = x_1 = -x_2$, and $x = 0$ is chosen at the center of the detection screen. The normalized second-order correlation function [5] is thus

$$\Delta g^{(2)}(x,-x) \equiv \Delta g^{(2)}(x) \propto |\widetilde{D^2}(2kx/z)|^2. \quad (20)$$

This result states that the deviation of the normalized intensity correlation function is proportional to the Fourier

transformation of the double-slit spatial pattern and thus the far-field interference pattern. It reveals that the diffraction pattern will be recovered if a dephaser is applied. However, for a decoherer, the far-field pattern is not recovered. For the decoherer, Eq. (15) is expressed as

$$\begin{aligned}\Delta G^{(2)}(x_1,x_2) &\equiv \sum_n \left| \int dx_1' dx_2' h^*(x_1,x_1') h(x_2,x_2') G_n{}^{(1)}(x_1',x_2') \right|^2 \\ &= \sum_n \left| 2\pi I_0 e^{ik\frac{(x_2^2-x_1^2)}{2z}} \widetilde{T}_n^2\left(\frac{k}{z}(x_1-x_2)\right)\right|^2, \end{aligned} \tag{21}$$

where $G_n^{(1)}(x_i',x_j')$ is the nth wave's first-order correlation function.

The deviation of the normalized intensity correlation function of the far-field intensity distribution for 500 different phase realizations is averaged using Eq. (18) and compared to the Fourier transformation of the double-slit transmission function,

$$I = 4W^2\left(\frac{W\sin\theta}{\lambda}\right)^{-2}\mathrm{sinc}^2\left(\frac{W\sin\theta}{\lambda}\right)\cos^2\left(\frac{\pi D\sin\theta}{\lambda}\right), \tag{22}$$

where W is the width of slits, D is the distance between the center of two slits, and λ is the wavelength (30 pm). The angle θ is related to detector position by $\theta = \frac{2x}{d}$, where x is the distance to the center and d is the distance between the detection screen and the double slit. The result is given in Fig. 6.

The relationship between Figs. 5 and 6 is that two example patterns of the 500 total simulations are shown for the dephaser in Figs. 5(a) and 5(c), which correspond to the intensity correlation function in Fig. 6(a). In the same way the decoherer patterns in Figs. 5(b) and 5(d) correspond to Fig. 6(b). The effect of applying the intensity correlation function on the patterns that underwent dephasing [blue in Fig 6(a)] is in agreement with the theoretical double-slit diffraction pattern (orange) which confirms Eq. (17). This phenomenon has been observed in the optical regime [5] and we have now shown that it is possible to be observed in the matter-wave regime. In Fig. 6(b) the intensity correlation function for the decoherer shows the absence of a double-slit pattern. Thus, we have a method to tell the difference between decoherence and dephasing in a process.

The visibility of the intensity correlation functions is also calculated since it is related to the entropy increase in the simulation. The relationship is model dependent, but it is monotonic within the model considered. We investigated the relation and found a confidence range to estimate the sensitivity of our method. The results are presented in Fig. 7.

In summary, the increase of entropy (Fig. 3) is one-to-one related to the absence of a double-slit diffraction pattern in the intensity correlation function (Fig. 6), and such an absence identifies the presence of a time-irreversible process. This finding regarding the change in entropy matches Zurek's description of decoherence very well. Zurek [23] explains that "Observers can be ignorant of phases for reasons that do not lead to an imprint of the state of the system on the environment. … Transfer of information about a decohering

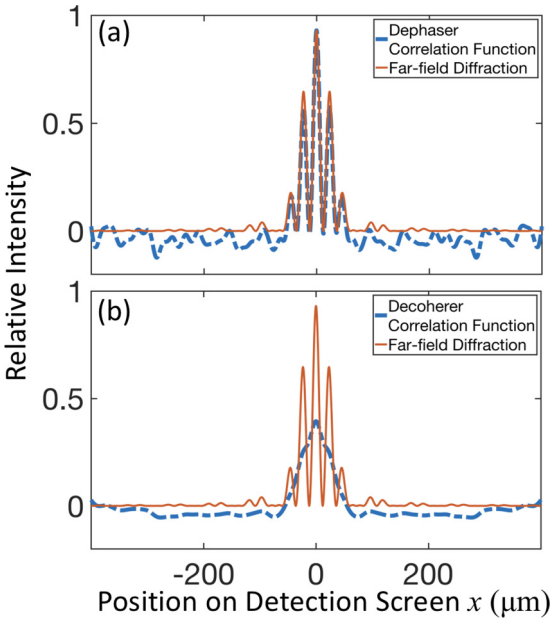

FIG. 6. Double-slit pattern recovery. A comparison is made between the deviation of the intensity correlation function and the corresponding far-field diffraction pattern [Eq. (22)] of the double slits. The orange solid curve is the far-field double-slit diffraction pattern. The dashed blue curve is the intensity correlation function averaged over (a) 500 dephaser realizations and (b) 500 decoherer realizations. In (a), the deviation recovers the diffraction pattern while in (b) this is not the case.

system to the environment is essential, and plays a key role in the interpretation." That is to say, if information is transferred by decoherence to the environment, then the information entropy will increase. "Hence, in the case of dephasing …,

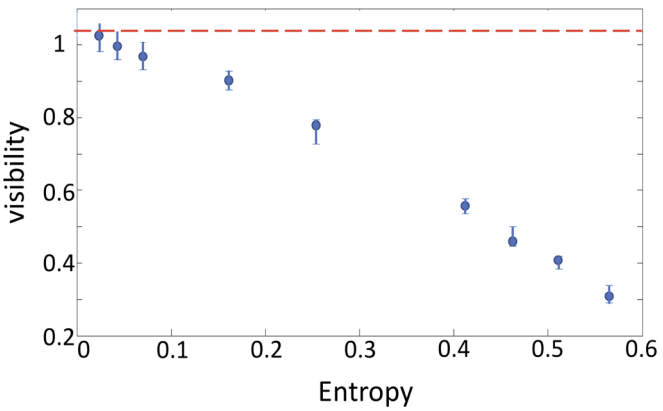

FIG. 7. Entropy and the visibility: their relationship in our model. The data are generated by calculating the visibility of the intensity correlation function for different strengths of the decoherence process in the system. The intensity correlation functions are based on 500 measurements for every decoherence strength. A stronger decoherence process produces more decoherence and a corresponding higher entropy. Blue dots with lower visibility indicate more decoherence. The error bar is a 95% confidence interval. The dashed red line is the measured visibility value for the pure dephasing process. This figure serves to indicate the sensitivity of the method.

information about the cause obtained … afterwards, suffices to undo the effect." In our example, the effect of the dephasing (the scrambling of the diffraction image) is undone by the correlation method presented here. "Decoherence relies on entangling interactions. … Thus neither prior nor posterior knowledge of the state of the environment is enough." Indeed, for our example, the correlation method does not recover the diffraction image for the case of decoherence.

In this context the interesting approach of Stibor *et al.* [24–26] to remove dephasing is relevant. In their method, correlation in space and time is used and experimentally shown to remove dephasing for externally applied fields. It is different from the present method in that a specific form of the dephasing fields is assumed, that it uses time explicitly, and that it does not evaluate decoherence.

The Hanbury-Brown–Twiss effect can also be compared with our method. First, it is useful to recall the difference between the classical and quantum Hanbury-Brown–Twiss (HBT) effect. The classical HBT effect is a wave phenomenon (that holds for one-particle experiments), while the quantum HBT effect depends on the bosonic or fermionic nature of the particle [27,28] (that holds for two-particle experiments). Our method can only be compared meaningfully to the classical HBT effect as we are using one-particle wave functions. We thus compare, for example, the second-order correlation function for collision-broadened thermal light to the second-order correlation function for electrons emanating from a double slit with a noisy phase (see the Appendix). There is no mathematically identical mapping between these second-order correlation functions.

For thermal light, the second-order correlation function can be expressed in terms of the first-order correlation function, $g^{(2)}(\tau) = 1 + |g^{(1)}(\tau)|^2$ [29], while for electrons that propagate from a double slit a similar relation is found by $g^{(2)}(x_1,x_2) = 1 + |\int dx_1' dx_2' h_1(x_1,x_1') h_2^*(x_2,x_2') g^{(1)}(x_1',x_2')|^2$ [this is our Eq. (11) normalized by $\langle I_1(x_1)\rangle\langle I_2(x_2)\rangle$]. A difference is that matter-wave propagation (with a quadratic dispersion relation) is not the same as light propagation (with a linear dispersion relation). Additionally, the light of thermal sources is considered to be continuous and not pulsed. The electron source is a double slit and is not continuous in space. Finally, our method distinguishes between dephasing and decoherence for electrons. Decoherence is a quantum property and not a wave property.

It is not clear at this point how general the intensity correlation function processing method is. All our numerical tests indicate that the method works when the dephaser pervades the entire wave function, with spatial fluctuations one order of magnitude (or more) smaller than the single slit width. This is the scenario discussed in multiple theoretical models [13,15,16,30,31] and experiments [10,17,18]. Other alternative setups such as an interferometer with a dephaser or decoherer in one arm can be considered. When a known static dephaser is placed in the other interferometer arm, dephasing and decoherence can be distinguished. On the other hand, when the dephaser only acts at the location of one slit, and no dephaser is present at the location of the other slit, the double-slit pattern is not recovered in the intensity correlation function. This is an example where the method fails. A more detailed study is required to identify both analytically and numerically what the validity range of the correlation method is. An additional experimental requirement is that multiple probability distributions must be recorded, each corresponding to different phase realizations. This can be done by decohering or dephasing the object as a function of the position. For example, the lateral position of the surface in Fig. 2 could be varied. For a position-dependent dephaser, it is expected that the diffraction pattern will be recovered, while for a decoherer (for example, based on image charge), the lateral position does not affect the diffraction image and the diffraction pattern will not be recovered. The correlation method is not expected to work in all cases. For example, if the surface acts as a homogeneous decoherer, there may be no position dependence. If the time dependence of the interaction between the electron and the surface is on the order of the electron-electron interaction time (≈10 fs) then a repetitive time-averaged accumulation of the probability distribution will yield identical results. In this case techniques exist that are developed for ultrafast electron diffraction and microscopy [32,33] where this time domain in now being reached [34].

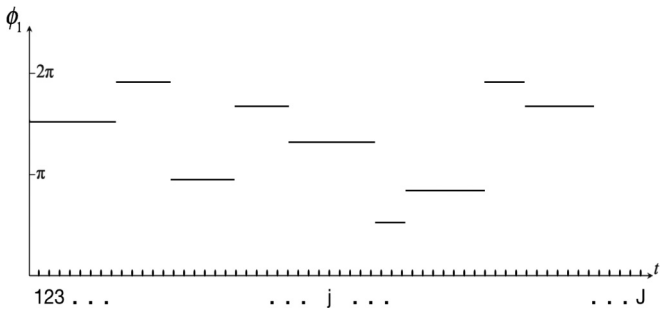

FIG. 8. Multistep function: the phase of emitted light by one atom in the thermal source. The atom is emitting light wave trains of a certain frequency and phase as the horizontal line segments indicate. A collision will reset its initial phase, which cause a "phase jump" in the figure. The length of each line is the temporal length of a wave train which is set by the free flight time of the atom. The length is an exponentially distributed random number with a mean free flight time τ_c. A temporal grid is shown in the figure to indicate the discretization of time (see text).

In conclusion, an alternative to holography or tomography is offered to distinguish dephasing from decoherence and thus identify time-reversible from time-irreversible processes. The visibility of intensity correlation functions can be analyzed to find the corresponding entropy change. In our model, visibility lower than 0.998314 (for which the corresponding entropy increase is 0.043) confirms the existence of a decohering process in the system with a 95% confidence level. Note that the sensitivity of the method varies with the model. This technique of using repetitive correlation measurements to distinguish between dephasing and decoherence is discussed in the context of electron matter optics, should be applicable to optics, and can lead to new experiments in both fields.

The authors wish to thank Wolfgang Schleich, Sam Keramati, and Eric Jones for discussions. This work was completed utilizing the Holland Computing Center of the University of Nebraska, which receives support from the Nebraska Research

Initiative. We gratefully acknowledge support by the U.S. National Science Foundation under Grant No. 1602755.

APPENDIX

Collision-broadened thermal light can be described as a summation of light waves emitted from numerous atoms. Those waves consist of many discrete wave trains. From one wave train to another, a sudden phase shift will occur due to atomic collisions. The length τ of each wave train is exponentially distributed as $p(\tau) = \frac{1}{\tau_c} e^{-\frac{\tau}{\tau_c}}$, where $p(\tau)$ is the probability of finding a wave train with length τ, and τ_c is the mean free flight time of atoms. The frequency of all emitted waves is assumed to be the same. To express this mathematically,

$$E(t) = A_0 e^{-i\omega t}(e^{i\phi_1(t)} + e^{i\phi_2(t)} + \cdots + e^{i\phi_n(t)}). \tag{A1}$$

Inside the equation is a summation of the fields of n atoms. In considering the first atom, for example, its field includes a multistep function as shown below.

The second-order correlation function is defined by

$$g^{(2)}(\tau) = \frac{\langle E^*(t)E^*(t+\tau)E(t)E(t+\tau)\rangle}{\langle E^*(t)E(t)\rangle\langle E^*(t)E(t)\rangle}, \tag{A2}$$

where $\langle\cdots\rangle$ is the average taken over a time much larger than the mean free flight time τ_c. To compare this calculation with our simulation for electrons, we rewrite the integral as a sum using a discretized time duration as labeled in Fig. 8. Thus, $t = t(j)$ and $\tau = \tau(\Delta j)$. The $g^{(2)}(\tau)$ function can be written as

$$g^{(2)}(\tau) = \frac{\sum_{j=1}^{J} E^*(j)E^*(j+\Delta j)E(j)E(j+\Delta j)/J}{\sum_{j=1}^{J} E^*(j)E(j)\sum_{j=1}^{J} E^*(j)E(j)/J^2}. \tag{A3}$$

Substituting the field expression Eq. (A1) into Eq. (A3) gives

$$g^{(2)}(\tau) = \frac{\sum_{j=1}^{J} |\sum_{i=1}^{n} e^{-i\omega t(j)} e^{i\phi_i(j)}|^2 |\sum_{i=1}^{n} e^{-i\omega t(j+\Delta j)} e^{i\phi_i(j+\Delta j)}|^2/J}{\sum_{j=1}^{J} |\sum_{i=1}^{n} e^{-i\omega t(j)} e^{i\phi_i(j)}|^2 \sum_{j=1}^{J} |\sum_{i=1}^{n} e^{-i\omega t(j)} e^{i\phi_i(j)}|^2/J^2}. \tag{A4}$$

However, in our simulation, the spatially dependent phase noise cannot be mapped identically onto the counterpart of the temporal stepped phase in the thermal light model. To illustrate this, consider the thought experiment modeled in our simulation (Fig. 9).

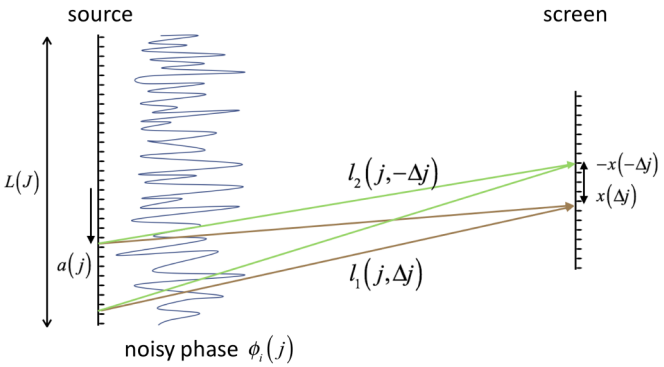

FIG. 9. Simulation schematic. A uniform source is placed on the double-slit plane (the double slit is removed). A noisy phase is applied. Discretized spatial coordinates are used. The green and red lines indicate the propagation path from the source $a(j)$ to the screen positions $x(\Delta j)$ and $-x(-\Delta j)$.

Discretized spatial coordinates $a = a(j)$ on the source and $x = x(\Delta j)$ on the screen are shown. Amplitudes on the source propagate from point j to point $\pm\Delta j$ and the path length l is a function of j and Δj. Using the path-integral formalism, fields on the screen are

$$E_i(x) = \sum_{j}^{J} e^{-i\frac{2\pi}{\lambda} l(j,\Delta j)} e^{i\phi_i(j)}, \tag{A5}$$

$$E_i(-x) = \sum_{j}^{J} e^{-i\frac{2\pi}{\lambda} l(j,-\Delta j)} e^{i\phi_i(j)}. \tag{A6}$$

Using the intensity correlation function,

$$g^{(2)}(x) = \frac{\langle I(x)I(-x)\rangle}{\langle I(x)\rangle\langle I(-x)\rangle}, \tag{A7}$$

and expressing this explicitly in discrete spatial coordinates, we find

$$g^{(2)}(\Delta j) = \frac{\sum_{i}^{n} \left|\sum_{j}^{J} e^{-i\frac{2\pi l(j,\Delta j)}{\lambda}} e^{i\phi_i(j)}\right|^2 \left|\sum_{j}^{J} e^{-i\frac{2\pi l(j,-\Delta j)}{\lambda}} e^{i\phi_i(j)}\right|^2/N}{\sum_{i}^{n} \left|\sum_{j}^{J} e^{-i\frac{2\pi l(j,\Delta j)}{\lambda}} e^{i\phi_i(j)}\right|^2 \sum_{i}^{n} \left|\sum_{j}^{J} e^{-i\frac{2\pi l(j,-\Delta j)}{\lambda}} e^{i\phi_i(j)}\right|^2/N^2}. \tag{A8}$$

This can now be compared with Eq. (A4). The summation order is different. For thermal light the random phase depends on j and $j + \Delta j$, while for electrons it depends only on j. For thermal light the time is dependent on $j + \Delta j$, while for electrons the position depends on j and Δj. The total number of summations is also different.

[1] M. A. Nielsen and I. L. Chuang, *Quantum Computation and Quantum Information* (Cambridge University Press, Cambridge, U.K., 2011).

[2] G. M. D'Ariano, M. G. A. Paris, and M. F. Sacchi, in *Advances in Imaging and Electron Physics*, edited by P. W. Hawkes, Vol. 128 (Academic Press, 2003), p. 205.

[3] R. P. Feynman, R. B. Leighton, and M. Sands, in *The Feynman Lectures on Physics* (Addison-Wesley, Reading, MA, 1965), Chap. 1.

[4] R. Bach, D. Pope, S.-H. Liou, and H. Batelaan, New J. Phys. **15**, 033018 (2013).

[5] L. Rui-Feng, Y. Xin-Xing, F. Yi-Zhen, Z. Pei, Z. Yu, G. Hong, and L. Fu-Li, Chin. Phys. B **23**, 054202 (2014).

[6] M. Brune, E. Hagley, J. Dreyer, X. Maître, A. Maali, C. Wunderlich, J. M. Raimond, and S. Haroche, Phys. Rev. Lett. **77**, 4887 (1996).

[7] C. J. Myatt, B. E. King, Q. A. Turchette, C. A. Sackett, D. Kielpinski, C. A. Sackett, C. J. Myatt, D. J. Wineland, C. Monroe, B. E. King, W. M. Itano, Q. A. Turchette, W. M. Itano, C. Monroe, and D. J. Wineland, Nature (London) **403**, 269 (2000).

[8] K. Hornberger, S. Uttenthaler, B. Brezger, L. Hackermüller, M. Arndt, and A. Zeilinger, Phys. Rev. Lett. **90**, 160401 (2003).

[9] L. Hackermüller, K. Hornberger, B. Brezger, A. Zeilinger, and M. Arndt, Nature (London) **427**, 711 (2004).

[10] P. Sonnentag and F. Hasselbach, Phys. Rev. Lett. **98**, 200402 (2007).

[11] J. Trost and K. Hornberger, Phys. Rev. Lett. **103**, 023202 (2009).

[12] E. R. Jones, R. A. Bach, and H. Batelaan, Eur. J. Phys. **36**, 065048 (2015).

[13] J. R. Anglin and W. H. Zurek, in *Dark Matter Cosmol.* Quantum Meas. Exp. Gravit. (Editions Fronti'eres, Gif-sur-Yvette, France, Les Arcs, Savoie, France, 1996), pp. 263–270.

[14] J. R. Anglin, J. P. Paz, and W. H. Zurek, Phys. Rev. A **55**, 4041 (1997).

[15] P. Machnikowski, Phys. Rev. B **73**, 155109 (2006).

[16] S. Scheel and S. Y. Buhmann, Phys. Rev. A **85**, 030101 (2012).

[17] F. Röder and A. Lubk, Ultramicroscopy **146**, 103 (2014).

[18] B. Barwick, G. Gronniger, L. Yuan, S.-H. Liou, and H. Batelaan, J. Appl. Phys. **100**, 074322 (2006).

[19] R. P. Feynman, Rev. Mod. Phys. **20**, 367 (1948).

[20] J. Cheng and S. Han, Phys. Rev. Lett. **92**, 093903 (2004).

[21] P. Kazemi, S. Chaturvedi, I. Marzoli, R. F. O'Connell, and W. P. Schleich, New J. Phys. **15**, 013052 (2013).

[22] J. W. Goodman, *Statistical Optics* (Wiley, 2000), pp. 41–44.

[23] W. H. Zurek, Rev. Mod. Phys. **75**, 715 (2003).

[24] A. Rembold, G. Schütz, W. T. Chang, A. Stefanov, A. Pooch, I. S. Hwang, A. Günther, and A. Stibor, Phys. Rev. A **89**, 033635 (2014).

[25] A. Günther, A. Rembold, G. Schütz, and A. Stibor, Phys. Rev. A **92**, 053607 (2015).

[26] A. Rembold, G. Schütz, R. Röpke, W. T. Chang, I. S. Hwang, A. Günther, and A. Stibor, New J. Phys. **19**, 033009 (2017).

[27] P. Lougovski and H. Batelaan, Phys. Rev. A **84**, 023417 (2011)

[28] Tom Jeltes *et al.*Nature (London) **445**, 402 (2007)

[29] R. Loudon, *The Quantum Theory of Light* (Oxford University Press, Oxford, 2000), pp. 110.

[30] A. Howie, Ultramicroscopy **111**, 761 (2011).

[31] A. Howie, J. Phys. Conf. Ser. **522**, 012001 (2014).

[32] B. J. Siwick, J. R. Dwyer, R. E. Jordan, and R. J. D. Miller, Science **302**, 1382 (2003).

[33] A. H. Zewail, Annu. Rev. Phys. Chem. **57**, 65 (2006).

[34] M. Gulde, S. Schweda, G. Storeck, M. Maiti, H. K. Yu, A. M. Wodtke, S. Schäfer, and C. Ropers, Science **345**, 200 (2014).